J. Fluid Mech. (2007), *vol.* 573, *pp.* 479–502. © 2007 Cambridge University Press
doi:10.1017/S0022112006003685 Printed in the United Kingdom

Oscillatory motion and wake instability of freely rising axisymmetric bodies

PEDRO C. FERNANDES, FRÉDÉRIC RISSO,
PATRICIA ERN AND JACQUES MAGNAUDET

Institut de Mécanique des Fluides, UMR 5502 CNRS-INP-UPS,
Allée du Prof. Camille Soula, 31400 Toulouse, France
risso@imft.fr, ern@imft.fr, magnau@imft.fr

(Received 2 May 2006 and in revised form 13 September 2006)

This paper reports on an experimental study of the motion of freely rising axisymmetric rigid bodies in a low-viscosity fluid. We consider flat cylinders with height h smaller than the diameter d and density ρ_b close to the density ρ_f of the fluid. We have investigated the role of the Reynolds number based on the mean rise velocity u_m in the range $80 \leqslant Re = u_m d/\nu \leqslant 330$ and that of the aspect ratio in the range $1.5 \leqslant \chi = d/h \leqslant 20$. Beyond a critical Reynolds number, Re_c, which depends on the aspect ratio, both the body velocity and the orientation start to oscillate periodically. The body motion is observed to be essentially two-dimensional. Its description is particularly simple in the coordinate system rotating with the body and having its origin fixed in the laboratory; the axial velocity is then found to be constant whereas the rotation and the lateral velocity are described well by two harmonic functions of time having the same angular frequency, ω. In parallel, direct numerical simulations of the flow around fixed bodies were carried out. They allowed us to determine (i) the threshold, $Re_{cf1}(\chi)$, of the primary regular bifurcation that causes the breaking of the axial symmetry of the wake as well as (ii) the threshold, $Re_{cf2}(\chi)$, and frequency, ω_f, of the secondary Hopf bifurcation leading to wake oscillations. As χ increases, i.e. the body becomes thinner, the critical Reynolds numbers, Re_{cf1} and Re_{cf2}, decrease. However, introducing a Reynolds number Re^* based on the velocity in the recirculating wake makes it possible to obtain thresholds Re^*_{cf1} and Re^*_{cf2} that are independent of χ. Comparison with fixed bodies allowed us to clarify the role of the body shape. The oscillations of thick moving bodies ($\chi < 6$) are essentially triggered by the wake instability observed for a fixed body: $Re_c(\chi)$ is equal to $Re_{cf1}(\chi)$ and ω is close to ω_f. In the range $6 \leqslant \chi \leqslant 10$ the flow corrections induced by the translation and rotation of freely moving bodies are found to be able to delay the onset of wake oscillations, causing Re_c to increase strongly with χ. An analysis of the evolution of the parameters characterizing the motion in the rotating frame reveals that the constant axial velocity scales with the gravitational velocity based on the body thickness, $\sqrt{((\rho_f - \rho_b)/\rho_f)\, gh}$, while the relevant length and velocity scales for the oscillations are the body diameter d and the gravitational velocity based on d, $\sqrt{((\rho_f - \rho_b)/\rho_f)\, gd}$, respectively. Using this scaling, the dimensionless amplitudes and frequency of the body's oscillations are found to depend only on the modified Reynolds number, Re^*; they no longer depend on the body shape.

1. Introduction

In numerous situations, bodies (bubbles, drops or particles) of size d evolve freely in a Newtonian fluid of viscosity μ. When the body density ρ_b is different from that of the fluid, ρ_f, the body moves relative to the fluid, say with velocity U. If the density ratio ρ_b/ρ_f is not large, the motion involves a coupling between the hydrodynamics (i.e. the disturbance flow induced by the body) and the body's degrees of freedom (i.e. its velocity and rotation rate). When the Reynolds number $Re = \rho_f U d/\mu$ is large enough for a significant wake to develop behind the body, complex behaviours may be observed. Here, we consider the simple case of a body rising in a fluid otherwise at rest under the action of buoyancy. The relevant velocity scale is then the gravitational velocity, and the Reynolds number becomes the Archimedes number, $Ar = \rho_f r_{eq}((\Delta\rho/\rho_f)\, g\, r_{eq})^{1/2}/\mu$, where the equivalent radius r_{eq} is that of a sphere of the same volume and $\Delta\rho = |\rho_f - \rho_b|$.

Investigations concerning either the particular case of a sphere or that of bodies of negligible thickness have been reported in the literature. Jenny, Dusek & Bouchet (2003, 2004) investigated the case of a sphere and described the various regimes that occur when Ar and ρ_b/ρ_f are varied. The instability of the rectilinear motion is caused by the instability of the sphere wake and the regime transitions depend on the density ratio, which influences the action of the wake on the body translation. Several studies have also been devoted to bodies of negligible thickness, either circular disks (Willmarth, Hawk & Harvey 1964; Stewart & List 1983; Field *et al.* 1997) or two-dimensional cards (Mahadevan 1996; Belmonte, Eisenberg & Moses 1998; Mahadevan, Ryu & Samuel 1999; Pesavento & Wang 2004; Andersen, Pesavento & Wang 2005*a*, *b*; Jones & Shelley 2005). Depending on the Archimedes number and the density ratio, fluttering, tumbling or chaotic motions are observed. In any case, the drift angle between the instantaneous body velocity and orientation reaches significant values, up to 180° in the tumbling regime. The existence of this drift angle has two main consequences. It strongly couples the wake structure to the body rotation. It also couples the body translation and rotation because of the tensorial nature of the dependence of the added-inertia forces and moments (Lamb 1932) on the body's linear and angular velocities. The large shape anisotropy therefore drastically changes the body's dynamics.

For axisymmetric geometries, the body shape can be characterized by the ratio, $\chi = d/h$, of the maximum diameter d and the dimension h measured in the direction parallel to the revolution axis. To our knowledge, oblate solid bodies of intermediate shape ($1 < \chi < \infty$) have not been considered yet. In contrast, many studies have been devoted to ellipsoidal rising bubbles, with aspect ratios ranging from 1 to 3. For diameters within 1.5–5 mm, regular oscillatory motions along either a plane zigzag or a helical path are commonly observed (Saffman 1956; Aybers & Tapucu 1969). Analysis of the bubble dynamics is more complicated than that for solid bodies. First, the bubble shape is coupled to its motion through the balance between flow-induced stresses and surface tension. Second, interfacial properties (and hence flow boundary conditions) can be strongly influenced by the presence of minute concentrations of surfactant. For bubbles in clean water, it has nevertheless been established both from experiment (Ellingsen & Risso 2001) and numerical simulations (Mougin & Magnaudet 2002) that shape fluctuations play no significant role in the regime of path oscillations that follows the rectilinear rise. After the initial acceleration stage, the bubble indeed maintains a constant ellipsoidal shape (with χ about 2) all along its oscillatory path. At variance with the solid-disk case, the drift angle between the bubble velocity and orientation remains very small at each instant.

The present work is a detailed experimental investigation of the behaviour of flat rising cylinders. The problem involves three dimensionless parameters. The density ratio is always close to unity whereas the Archimedes number is varied within the range 70–120, which includes the transition between the steady rectilinear rise regime and the periodic regime. The aspect ratio is varied from 2 to 20 with the goal of analysing the role of the shape anisotropy. In the range of parameters we consider, the dynamics are controlled by the interplay between inertia and vorticity. The relative inertia, which determines the ability of the body to react to hydrodynamic efforts, depends on the shape through the proper and added-inertia tensors for the body. The vorticity production, which is responsible for the generation of the boundary layer at the body surface and the wake behind it, also depends on the body shape. To disentangle the roles of the aspect ratio in these two phenomena, we shall compare experimental results obtained with a moving body with numerical results for the flow about the same fixed body.

The paper is organized as follows. Section 2 describes the experimental setup and procedure. Section 3 presents the technique used to obtain a three-dimensional description of the body's motion, including translation and rotation. Section 4 provides a complete characterization of the saturated oscillatory motions (in terms of frequency, amplitudes and phases) in the considered range of Archimedes numbers and aspect ratios. Then, § 5 discusses the onset of the path oscillations of moving bodies from a comparison with wake destabilization for fixed bodies. Finally, § 6 presents an attempt to collapse the results obtained for all aspect ratios by using a modified Reynolds number based on a velocity scale characteristic of the reverse flow in the near wake.

2. Experimental setup and procedure

The experimental procedure consists in tracking freely rising cylindrical bodies released from the bottom of a tank filled with salt water. Their three-dimensional displacement and orientation are accurately measured by means of two perpendicular travelling cameras (figure 1).

The bodies are flat cylinders manufactured from nylon rods. This material was chosen because it is easily workable and has a density, $\rho_b \approx 1.02\,\mathrm{g\,cm^{-3}}$, close to that of water. Diameters d (resp. heights h) range from 5 to 20 mm (resp. 1 to 5 mm) and are measured with an accuracy of ± 0.01 mm. The aspect ratio $\chi = d/h$, which varies from 1.5 to 20, is known with an accuracy better than ± 1 %. The body density was determined from floating tests performed in a 4 litre tank filled with salt water; the density of the solution was increased step by step by adding small quantities of salt. This method allowed us to determine the body density with an accuracy of $\pm 1 \times 10^{-4}\,\mathrm{g\,cm^{-3}}$. The density of the cylinders was found to range between 1.017 and $1.020\,\mathrm{g\,cm^{-3}}$.

The test section is a glass tank 1.70 m high with a square cross-section of 0.4 m width. The tank is located in a air-conditioned laboratory where the temperature is maintained at $21 \pm 1\,^{\circ}\mathrm{C}$. It is filled with water to which salt is added in order to adjust the density. The kinematic viscosity of the solution, close to $1.03 \times 10^{-6}\,\mathrm{m^2\,s^{-1}}$, was determined from chemical tables (Wolf, Brown & Prentiss 1981). Great care was taken to check the homogeneity of the solution within the tank. The temperature of the solution was monitored by means of two thermocouples located at the bottom and the top of the tank; the maximum temperature difference was always less than 0.5°C. Furthermore, the density of the solution was measured by means of a densimeter (KEM DA-310M, Mettler Toledo/Kyoto Electonics): 10 ml samples were frequently taken from both the top and bottom of the tank and their density was determined with an accuracy of $\pm 1 \times 10^{-4}\,\mathrm{g\,cm^{-3}}$. No stratification took place in the tank,

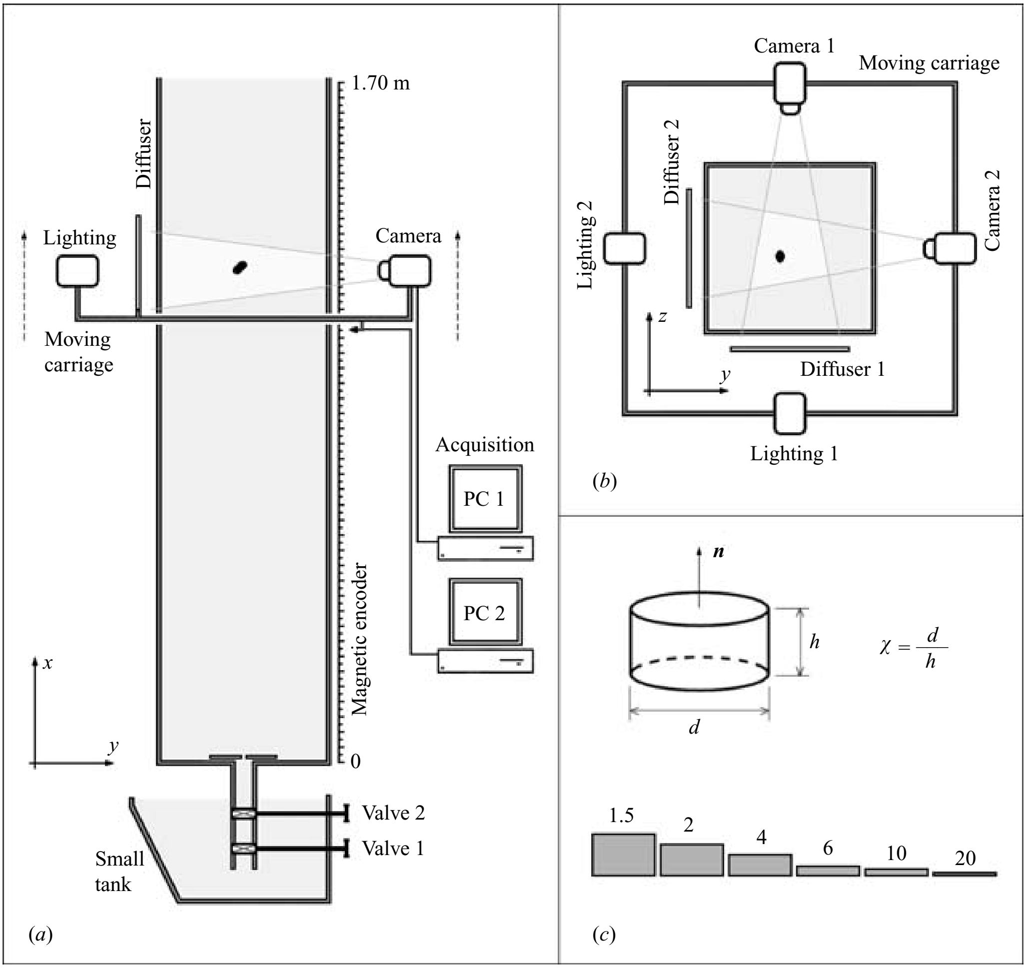

FIGURE 1. Schematic of the experimental setup. (*a*) Side view; (*b*) top view; (*c*) cylinders.

since the density difference between the top and the bottom was always less than $3 \times 10^{-4}\,\mathrm{g\,cm^{-3}}$.

Taking into account the errors in both the body and fluid densities, the density difference $\rho_f - \rho_b$ is known to an accuracy of $\pm 3 \times 10^{-4}\,\mathrm{g\,cm^{-3}}$. This allows us to investigate small density differences close to $(\rho_f - \rho_b)/\rho_f \simeq 10^{-2}$, i.e. density ratios ρ_b/ρ_f which differ from unity by only 1 %. Finally, the Archimedes number,

$$Ar = \frac{d}{\nu}\sqrt{\frac{3}{16}\,\frac{\rho_f - \rho_b}{\rho_f}\,gh},$$

is known to an accuracy of ±5 % and ranges from 70 to 120.

For each experimental run, the rise of a single cylinder corresponding to given Ar and χ values was investigated. The cylinder was released from the bottom of the tank using an original shutter consisting of two horizontal plates sliding in opposite directions. We checked that the initial conditions (the cylinder's inclination and the velocity disturbances) have no influence on the final periodic motion. Nevertheless, the cylinders were released gently and face up (with an inclination less than 10°).

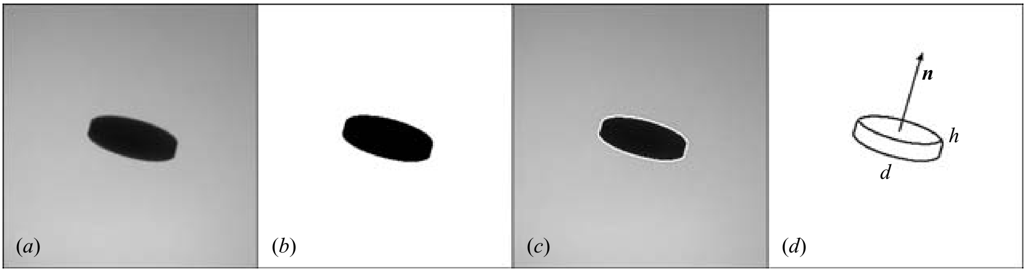

FIGURE 2. (*a*) Raw image of the body given by a camera; (*b*) the image after subtraction of the background image and binarization; (*c*) the detected contour superimposed on the raw image; (*d*) the ideal cylinder located and oriented as calculated from the contour.

The rise of the cylinders was then followed by two perpendicular travelling cameras and lights, the elevation of which was recorded by means of a high-accuracy (±5 μm) magnetic encoder. The magnetic encoder and cameras were synchronized and the acquisition of images was carried out at 10 Hz, which ensured that at least 25 images were recorded during each period of the body's oscillation.

3. Determination of the body's position and orientation

In this section we describe the image- and signal-processing techniques used to determine the time evolution of the coordinates of the body centre and the angles defining the orientation of its axis.

The two perpendicular cameras provide pairs of digital images. Since we used back lighting, each image (756 × 566 pixels in 256 grey levels) shows the projection of the body shadow in the visualization plane (figure 2*a*). Before each test, reference images were recorded, namely the background image in the absence of any body and a set of calibration images of a metal cylinder at various locations in the field of view. The first step of the image processing consists in subtracting the background image from the current image. Then a threshold is applied in the grey scale to obtain a binarized image in which the body shadow is black and the background is white (figure 2*b*). Finally the body contour, defined as a set of 600 adjacent pixels, is obtained as the border between the black and white regions (figure 2*c*). This method ensures an accuracy in the detection of each contour point of ±1 pixel. Then, the coordinates of the contour points are converted from pixels to millimetres using the calibration images. The linear variation in the optical scale factor with the distance from the focal planes is taken into account by an iterative procedure that uses the information supplied by the two cameras.

The coordinates of the body centre in the vertically moving camera frame (x_{cam}, y, z) are calculated as the isobarycentre of the contour points, with an accuracy of $\pm 1/2\,\text{pixel} = \pm 0.08\,\text{mm}$, better than that of each individual contour point because of the large number of points involved in their calculation. Figure 3(*a*) presents typical temporal evolutions of the horizontal coordinates y and z, showing an oscillatory behaviour. The vertical coordinate in the laboratory frame, x, is calculated by adding to x_{cam} the vertical coordinate of the cameras given by the magnetic encoder. Since the accuracy of the magnetic encoder (±5 μm) is far better than that of the contour detection, the accuracy in the vertical coordinate x is the same as that of the horizontal coordinates. Figure 3(*b*) shows the temporal evolution of $x - u_m t$, where u_m is the final mean rise velocity. We observe that after the initial accelerating stage,

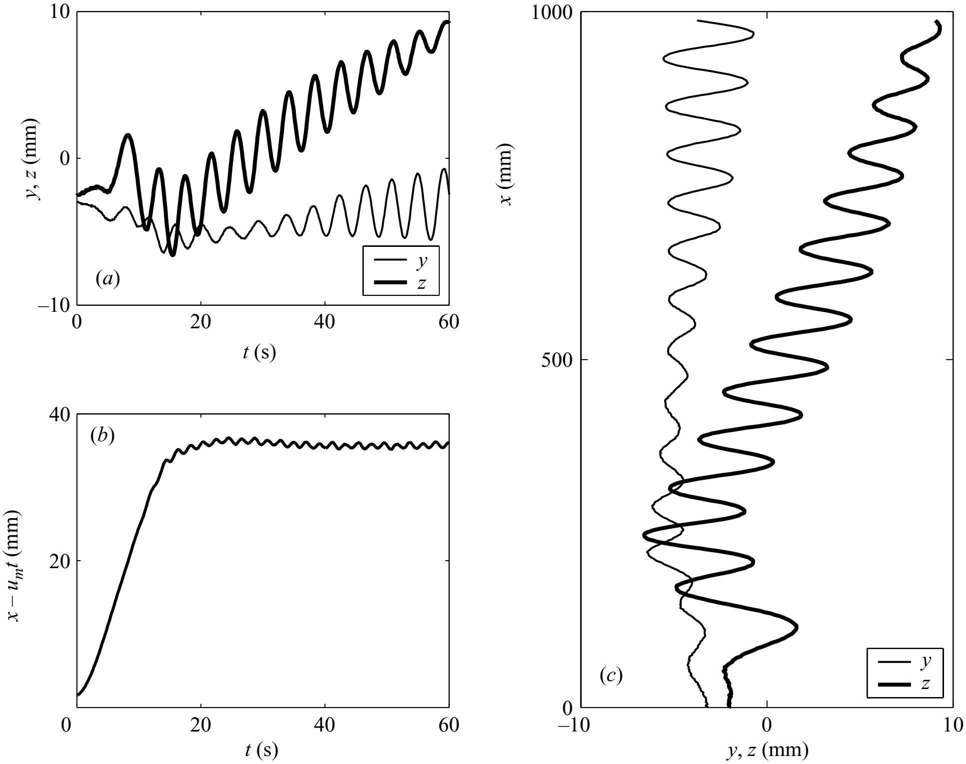

FIGURE 3. Measured coordinates of the body centre ($\chi = 7$, $Ar = 90$): (*a*) horizontal displacements; (*b*) vertical displacement; (*c*) projection of the trajectory onto the (x, y)-plane and the (x, z)-plane.

small oscillations are also measured along the vertical direction. The complete three-dimensional trajectory of the body in the laboratory frame is shown in figure 3(*c*).

The image processing also provides the orientation of the revolution axis of the body, which is defined by the unit vector $\boldsymbol{n}$ (figure 2*d*), whose coordinates are n_x, n_y, n_z. From each detected contour, we determined the 2×2 geometrical inertia tensor corresponding to the body's projection onto the corresponding vertical plane (the (x, y)-plane for camera 1, the (x, z)-plane for camera 2). Then we calculated its eigenvalues and eigenvectors. The direction of the projection of the body axis is given by the eigenvector associated with the largest eigenvalue. From each pair of images we thus obtained the angle θ_y (resp. θ_z) between the projection of the body axis onto the (x, y)-plane (resp. (x, z)-plane) and the vertical direction:

$$\cos\theta_y = \frac{n_x}{\|\boldsymbol{n} - n_z \boldsymbol{e_z}\|}, \tag{3.1}$$

$$\cos\theta_z = \frac{n_x}{\|\boldsymbol{n} - n_y \boldsymbol{e_y}\|}, \tag{3.2}$$

where $\boldsymbol{e_x}$, $\boldsymbol{e_y}$ and $\boldsymbol{e_z}$ are the unit vectors of the laboratory frame. Knowledge of θ_y and θ_z, which are determined to an accuracy of $\pm 0.75°$, is sufficient to determine the orientation $\boldsymbol{n}$ of the body axis.

The present image-processing technique provides an accurate measurement of five of the six degrees of freedom of the body, namely x, y, z, θ_y and θ_z. It is unlikely that

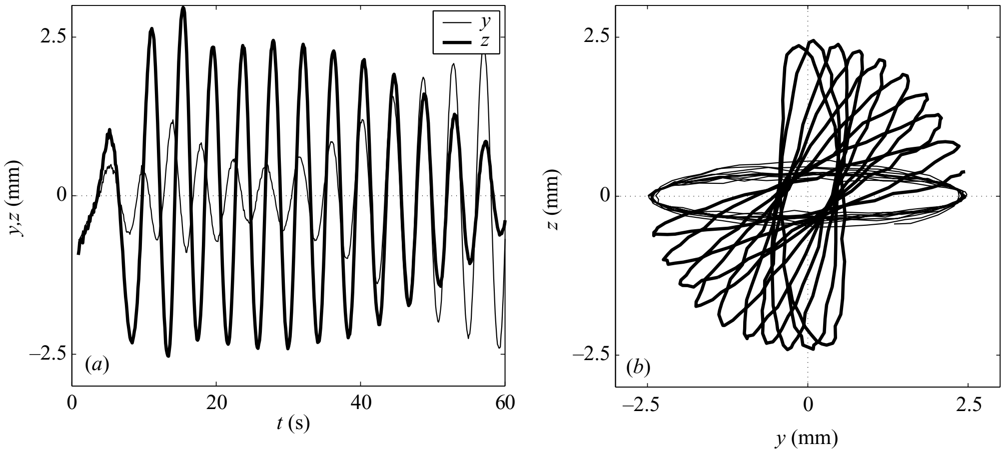

FIGURE 4. Removal of the weak horizontal drift and slow rotation (same run as in figure 3). (*a*) Horizontal displacements after the filtering of the low-frequency drift; (*b*) top view of the body path before (thick line) and after (thin line) the removal of the low-frequency rotation.

rotation about the symmetry axis, which we did not determine, played a significant role since it was always too small to be noticed by visual inspection. Moreover, as we shall see later, the body dynamics are essentially two-dimensional.

Figure 3 shows that the body motion involves different contributions: the vertical mean rise velocity, oscillations at a constant frequency and a weak horizontal drift. This drift is small since the average horizontal displacements were always observed to be less than 2 % of the vertical displacement; moreover, it was neither reproducible nor related to the governing parameters Ar and χ. Consequently, we decided to eliminate it by filtering out the low frequencies in the signals $x(t)$, $y(t)$ and $z(t)$. Figure 4(*a*) shows the filtered time evolution of the horizontal coordinates for the same case as in figure 3; $y(t)$ and $z(t)$ now oscillate about zero. However, their amplitudes are not converging towards constant values as expected whenever the path instability is saturating. Inspecting the trajectory from the top (figure 4*b*) reveals that this apparent evolution of the amplitudes is actually due to a slow rotation of the trajectory about a vertical axis. As for the horizontal drift, this rotation was not reproducible and was always weak (more than 50 times slower than the main oscillations); it was successfully eliminated by the following method. The measured horizontal coordinates can be described as harmonic functions with amplitudes that vary slowly in time:

$$y(t) = A_y(t)\sin(\omega t + \beta_y), \tag{3.3}$$

$$z(t) = A_z(t)\sin(\omega t + \beta_z). \tag{3.4}$$

The amplitudes $A_y(t)$ and $A_z(t)$, the phases β_y and β_z and the angular frequency ω are determined using the Hilbert transform. The principal directions of the oscillations can be calculated at each instant from the values of $A_y(t)$, $A_z(t)$, β_y and β_z (see Ellingsen & Risso 2001 for more details). Then a rotation about the vertical axis is applied in order to align the y-axis with the principal direction of oscillation. Figure 5 shows that in this new frame the horizontal oscillations reach constant amplitudes after the initial transient. We also note that, from a top view, the trajectory is now an ellipse, the major axis of which is aligned with the y-axis (figure 4*b*).

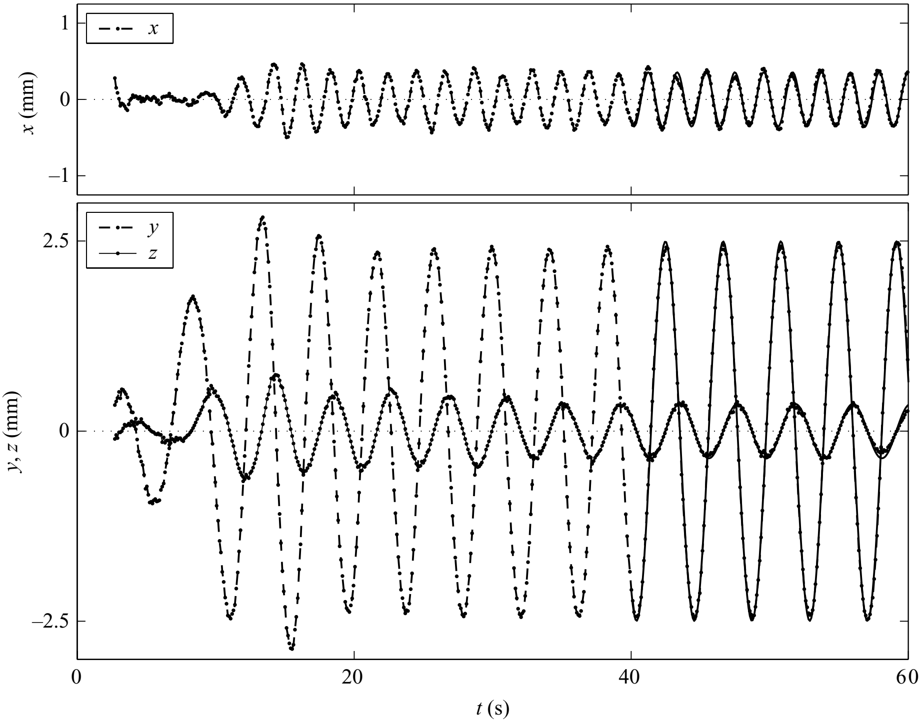

FIGURE 5. Body self-sustained oscillations in the principal frame (same run as in figure 3): evolution of the body-centre coordinates (dashed line, measurements; solid line starting at $t = 40$ s, the fit using (3.5)–(3.7)).

Of course, the low-frequency perturbations also affect the evolution of the body orientation. In the laboratory frame, the oscillations of θ_y and θ_z are always about zero, so no high-pass filtering is needed. However, their amplitudes do not reach constant values and the suppression of the low-frequency rotation is necessary. We applied the above procedure to the signals $\theta_y(t)$ and $\theta_z(t)$ and found the same principal frame of oscillations. Figure 6 shows that, in this frame, the amplitudes of θ_y and θ_z also reach constant values.

The low-frequency trajectory shift and rotation were also observed for rising bubbles by Ellingsen & Risso (2001). They are probably mainly due to weak residual large-scale motions, which cannot be totally avoided in a large tank. However, it might well be that part of these low-frequency contributions is intrinsically linked to the dynamics of the system (we shall come back shortly to this in § 5). Nevertheless they are so small that their level is at best comparable with that of the erratic displacements induced by the experimental defaults. Therefore we are not in a position to explore this possibility at the present stage. We have at least ensured, though, that the influence of these low-frequency contributions on the long-term body dynamics is negligible, since the results obtained after their removal are reproducible whereas these slow motions are not. In the following, these slow motions have been systematically eliminated and we shall call the laboratory frame the principal frame of oscillation.

After the initial transient, the measured body motions can be described by five harmonic functions,

$$x(t) = \widetilde{x}\,\sin(2\omega t - \phi_x) + u_m t, \tag{3.5}$$

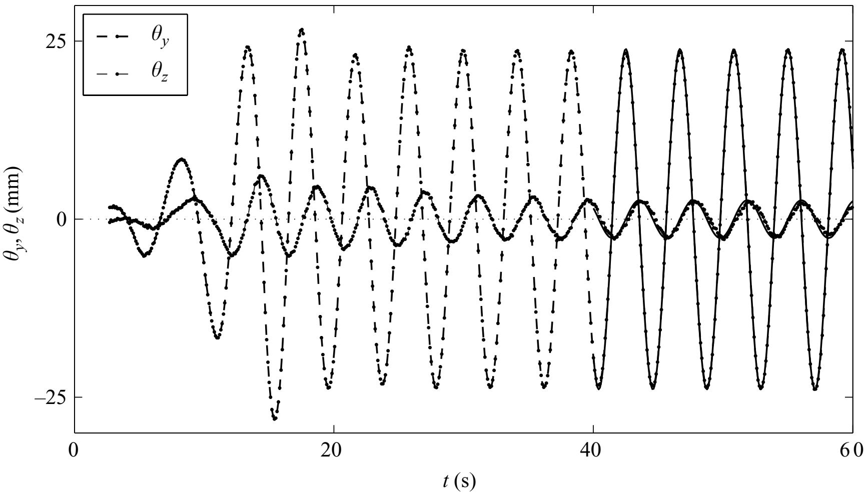

FIGURE 6. Body self-sustained oscillations in the principal frame (same run as in figure 3): inclination of the body axis (dashed line, measurements; solid line starting at $t = 40$ s, the fit using (3.8)–(3.9)).

$$y(t) = \widetilde{y}\ \sin(\omega t - \phi_y), \tag{3.6}$$

$$z(t) = \widetilde{z}\ \sin(\omega t - \phi_z), \tag{3.7}$$

$$\theta_y(t) = \widetilde{\theta}_y\ \sin(\omega t), \tag{3.8}$$

$$\theta_z(t) = \widetilde{\theta}_z\ \sin(\omega t - \psi_z), \tag{3.9}$$

which involve 11 parameters, the five amplitudes $\widetilde{x}, \widetilde{y}, \widetilde{z}, \widetilde{\theta}_y, \widetilde{\theta}_z$, the four relative phases $\phi_x, \phi_y, \phi_z, \psi_z$, the angular frequency ω and the mean rise velocity u_m. Their values are obtained by fitting the above harmonic functions to the measured signals. Figures 5 and 6 show that (3.5)–(3.9) accurately describe the measurements after the oscillations have reached a constant amplitude ($t > 40$ s in this example). From this description, linear and angular velocities or accelerations can easily be obtained analytically with a much higher accuracy than if they were determined using the numerical differentiation of data points.

4. Kinematics of freely moving bodies

Since the density ratio is fixed to a value close to unity, the characteristics of the body motions only depend on the Archimedes number and the aspect ratio. In this section, we present and discuss the measured characteristics of the motion for $70 \leqslant Ar \leqslant 120$ and $1.5 \leqslant \chi \leqslant 10$.

The mean rise velocity u_m is observed to range from 8 to 35 mm s^{-1} while the corresponding Reynolds number, $Re = u_m d/\nu$, ranges from 90 to 320. Figure 7 shows that Re depends very weakly on χ and increases almost linearly with the Archimedes number. Since the Reynolds number enables us to compare our experimental results with those for a fixed body placed in a uniform stream of velocity u_m, it will be used hereafter in place of the Archimedes number. Note that Re/Ar is proportional to the ratio of the rise velocity u_m and the gravitational velocity $u_g = \sqrt{(\Delta\rho/\rho_f)\,gh}$. When the body rises steadily along a rectilinear path, the axial body-drag coefficient equals $2u_g^2/u_m^2$ and is thus proportional to Ar^2/Re^2. For oscillating bodies, Ar^2/Re^2 yields the

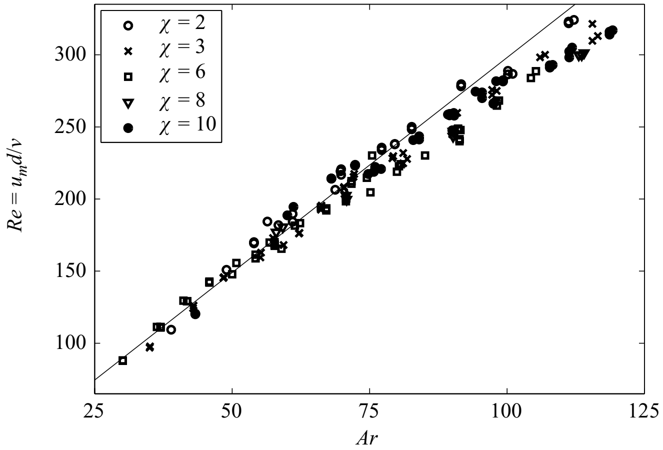

FIGURE 7. Reynolds number vs. Archimedes number for various aspect ratios (the line corresponds to $C_d = 1.2$).

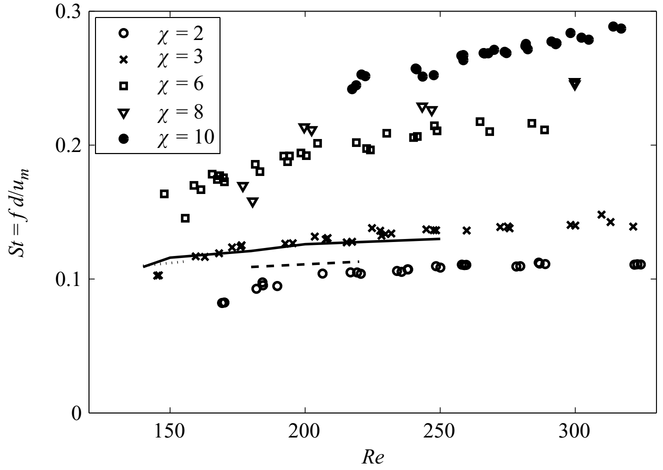

FIGURE 8. The dimensionless frequency given by the Strouhal number as a function of the Reynolds number. The symbols represent the experimental results for freely rising bodies with aspect ratios $\chi = 2$, 3, 6, 8 and 10. The lines correspond to numerical simulations of the flow around fixed bodies: dashed line, $\chi = 2$; dotted line, $\chi = 6$; solid line, $\chi = 10$ (note that for a fixed sphere St is about 0.135 at $Re = 300$).

vertical mean drag coefficient, which remains close to 1.2 over the present parameter range.

When oscillations are observed, both the body-axis inclination and the horizontal velocity have a well-defined frequency, $f = \omega/2\pi$, whereas the vertical velocity oscillates at twice this frequency (figure 5). The measured values of f range between 0.2 and 0.4 Hz. Figure 8 shows the evolution of the Strouhal number, $St = fd/u_m$, which is the ratio of the body diameter d and the path wavelength, $\lambda = u_m/f$. For a given aspect ratio, the Strouhal number varies weakly with the Reynolds number. It is almost constant for the thickest bodies, indicating that the wavelength λ increases proportionally with the body size (d or h). The Strouhal number, however, increases strongly with the aspect ratio.

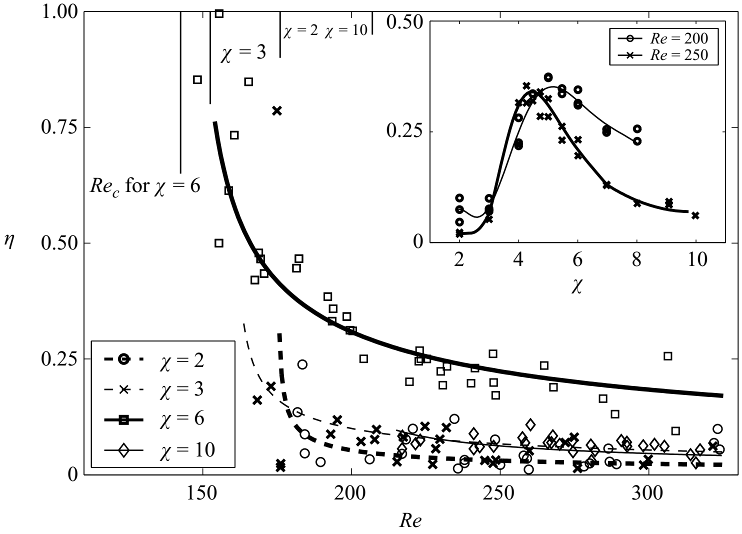

FIGURE 9. Ratio $\eta = \widetilde{z}/\widetilde{y}$ of the amplitudes of the horizontal body displacements ($\eta = 0$, plane zigzag; $\eta = 1$, circular helix). The vertical lines indicate the onset at Re_c of the oscillatory motions for each aspect ratio.

The horizontal body displacements are characterized by the amplitudes of the major, $\widetilde{y}$, and minor, $\widetilde{z}$, oscillations. Depending on the ratio $\eta = \widetilde{z}/\widetilde{y}$, the trajectory can range from a plane zigzag ($\eta = 0$) to a circular helix ($\eta = 1$). The top view of the body trajectory, given in figure 4(*b*), shows that the corresponding path is actually an elliptical helix ($0 < \eta < 1$). We also calculated the ratio of the major and minor amplitudes of the body-orientation oscillations and found that the values of $\widetilde{\theta}_z/\widetilde{\theta}_y$ are the same as those of $\eta = \widetilde{z}/\widetilde{y}$. In figure 9, the values of η are plotted against the Reynolds number. For each aspect ratio, η starts from a maximum value just above the onset, Re_c, of the path oscillations (which is indicated by a vertical line at the top of the figure) and then decreases as Re increases. Note that the behaviour observed near onset has to be taken with some caution, for two reasons: (i) the measured amplitudes are small and close to the experimental uncertainty; (ii) since if the bifurcation is supercritical the growth rate of the instability is likely to tend towards zero as Re tends towards Re_c, the tank may not be high enough to reach the final saturated amplitude. The inset in figure 9 shows the evolution of η for Reynolds numbers 200 and 250: both the thickest ($\chi = 2, 3$) and thinnest bodies ($\chi = 9, 10$) experience quasi-planar zigzagging motions ($\eta < 0.20$), whereas for intermediate aspect ratios the path becomes more helical ($\eta \approx 0.35$). Nevertheless, above $Re = 200$, η never exceeds 0.35, indicating that the trajectories are, rather, of the zigzag type. In the following we therefore consider a two-dimensional description of the body motion in a vertical plane corresponding to the three dominant degrees of freedom, x, y and θ_y; (3.7) and (3.9) are no longer considered, nor are the secondary parameters $\widetilde{z}$, $\widetilde{\theta}_z$, ϕ_z and ψ_z.

Figure 10 shows the amplitude of the body-axis inclination, $\widetilde{\theta}_y$, versus the Reynolds number. For all aspect ratios the behaviour is qualitatively similar. Below the critical Reynolds number Re_c the body rises steadily and $\widetilde{\theta}_y = 0$. Beyond Re_c, oscillations occur and the amplitude $\widetilde{\theta}_y$ increases with Re. The evolution of Re_c with aspect ratio is plotted in the inset. It was determined as the average of the value corresponding to the last measured stable case and that of the first unstable one. We observe that

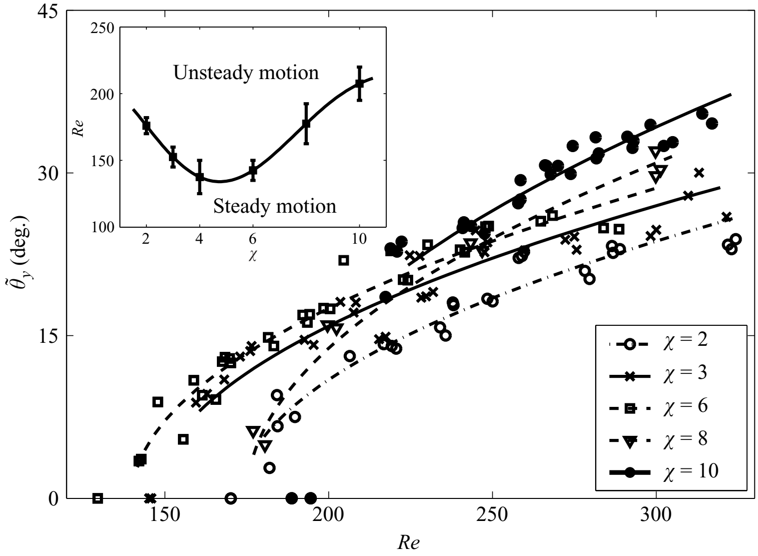

FIGURE 10. Amplitude of the body-axis inclination $\widetilde{\theta}_y$, vs. the Reynolds number for $\chi = 2$, 3, 6, 8 and 10 (the curves correspond to fits of the experimental data for each aspect ratio).

Re_c depends nonlinearly on the aspect ratio: it first decreases as χ is increased from 1.5 to 5, reaches a minimum and then increases as χ increases further. This complex behaviour will be discussed in § 5. The amplitude of the inclination angle is of the same order for all aspect ratios; the thinnest bodies start oscillating at a larger Reynolds number but the increase of their amplitude with Re is then stronger.

Concerning horizontal displacements, the measured amplitudes of the body-centre displacements $\widetilde{y}$ range from 0.15 to 6 mm. The onset condition for the oscillations of the body's displacement is the same as that for the body's orientation. Similarly to the fact that there is a unique frequency of oscillation ω, there is a unique threshold $Re_c(\chi)$. Figure 11 displays $\widetilde{y}/d$ as a function of $Re - Re_c$. The curves corresponding to the various aspect ratios have different magnitudes and slopes, which do not evolve monotonically with χ. As will be confirmed later, this indicates that y is not the most appropriate variable with which to analyse the bifurcation.

To complete the description of the horizontal oscillations, we need the phase difference ϕ_y between y and θ. In a preliminary paper (Fernandes *et al.* 2005), we presented and discussed the phase difference $\Delta\phi = \pi/2 - \phi_y$, which provides a description of the inclination of the body to the path. For thick bodies ($\chi \approx 2$) $\Delta\phi$ is close to zero. As the aspect ratio is increased, $\Delta\phi$ continuously increases up to a value slightly larger than $\pi/2$. While $\Delta\phi$ depends strongly on the body's aspect ratio, it depends only weakly on the Reynolds number. We also showed that the evolution of $\Delta\phi$ with χ cannot be obtained from the irrotational-flow approximation, which predicts $\Delta\phi = \pi$ whatever the aspect ratio; therefore it is clear that the wake plays a major role in these oscillatory motions.

It now remains to consider the characteristics of the oscillations in the vertical direction ($\widetilde{x}$ and ϕ_x). For the thickest bodies ($\chi \leqslant 3$), the experimental results show that $\widetilde{x}$ remains negligible whatever the Reynolds number. Beyond $\chi = 3$, $\widetilde{x}$ is an increasing function of both Re and χ. In any case, $\widetilde{x}$ remained moderate since the maximum measured value was $0.07d$ ($\approx 0.2\widetilde{y}$), for $\chi = 10$ and $Re = 320$. Hence it seems that there is a strong connection between $\Delta\phi$ and $\widetilde{x}$, suggesting that the body motion

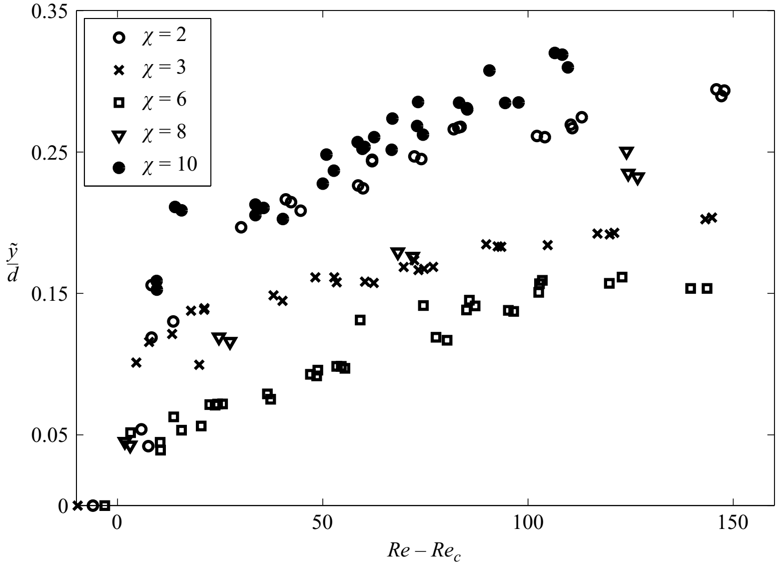

FIGURE 11. Amplitude of the horizontal displacement of the body centre $\tilde{y}/d$ vs. $Re - Re_c$ for $\chi = 2$, 3, 6, 8 and 10.

may appear simpler in a reference frame rotating with the body. Thus we make use of two different systems of axes, both of which have their origin fixed in the laboratory. The first is the Galilean laboratory frame with fixed axes (x, y); with this choice the components of the buoyancy do not vary in time. The second one makes use of axes X, Y rotating with the body, X being the direction parallel to the body axis; the boundary conditions at the body surface are then stationary, which in particular implies that the components of the proper and added-inertia tensors remain constant. Figure 12 shows the body-centre velocity in the two reference frames for a case where significant vertical oscillations are observed ($\chi = 10$, $Re = 270$). Figure 12(a) shows the vertical, $u_x = \mathrm{d}x/\mathrm{d}t$, and horizontal, $u_y = \mathrm{d}y/\mathrm{d}t$, components in the laboratory frame. Figure 12(b) shows the axial, u_X, and lateral, u_Y, components of the velocity projected onto the rotating frame. We see that there are no measurable velocity fluctuations in the direction parallel to the body axis. This conclusion holds throughout the investigated range of parameters. Hence in the rotating frame, the description of the body motion reduces to

$$u_X(t) = \overline{u_X}, \tag{4.1}$$

$$u_Y(t) = \widetilde{u_Y}\,\sin(\omega t - \phi_Y), \tag{4.2}$$

$$\theta_y(t) = \widetilde{\theta}_y\,\sin(\omega t). \tag{4.3}$$

From a mathematical point of view, one may note that if $u_Y(t)$ and $\theta_y(t)$ are harmonic functions, $u_y(t)$ and $u_x(t)$ cannot be so because the rotation of one reference frame with respect to the other involves nonlinear terms such as $u_y\,\cos(\theta_y)$. Indeed, a careful examination of the power spectrum of u_y (resp. u_x) shows a tiny secondary peak at 3ω (resp. 4ω); each peak has an amplitude which is 0.3 % of the primary peak. No comparable secondary peak was observed in the spectrum of u_Y, confirming that the rotating frame is better suited for the description of the body motion. Note, however, that the secondary harmonics contain so little energy that we obtained the same values for the motion parameters by fitting exact harmonic functions to the experimental results either in the laboratory frame or in the rotating frame. The

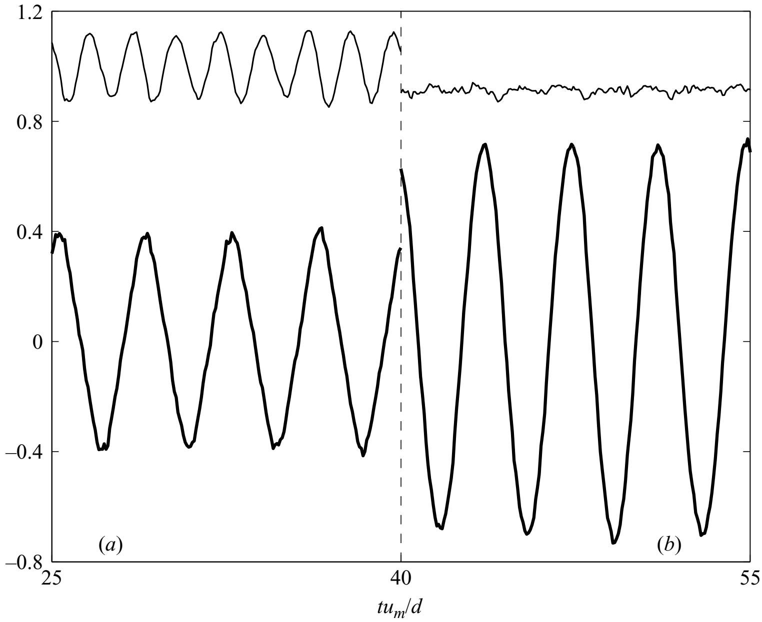

FIGURE 12. Temporal evolution of the body-centre velocity in two different reference frames. (*a*) Laboratory frame: thin line, u_x/u_m; thick line, u_y/u_m. (*b*) Rotating frame: thin line, u_X/u_m; thick line, u_Y/u_m.

evolution of the parameters that characterize the motion in the rotating reference frame will be presented and discussed in § 6.

5. Comparison between the wakes of moving and fixed bodies

A fixed body immersed in a uniform stream of constant velocity u_m represents the reference situation in which the six degrees of freedom of the body are blocked. It is of interest to compare the onset and frequency of the oscillations of moving bodies with those of the wake past fixed bodies. The linear stability of a fixed-sphere wake ($\chi = 1$) and a fixed-disk wake ($\chi = \infty$) was first studied by Natarajan & Acrivos (1993). In the case of a sphere, their results were confirmed and extended using direct numerical simulations (Johnson & Patel 1999; Ghidersa & Dusek 2000) and experiments (Provansal & Ormières 1998; Schouveiler & Provansal 2002). The scenario is the same for the two types of body. At low enough Reynolds number, the flow is steady and axisymmetric. Beyond a first critical Reynolds number Re_{cf1} the axial symmetry is broken by a regular bifurcation (i.e. a bifurcation for which the growth rate $e^{\sigma t}$ of the disturbance is purely real); the flow remains steady and symmetric relative to a plane that contains the body axis. Beyond a second critical Reynolds number $Re_{cf2} > Re_{cf1}$ the flow becomes unsteady owing to a Hopf bifurcation, and oscillating velocities are observed in the wake.

To our knowledge, no results are available for the body shapes considered here. To allow relevant quantitative comparisons with our experiments, we performed direct numerical simulations of the flow past flat cylinders with aspect ratios 2, 3, 4, 6 and 10. We used the finite-volume code JADIM developed by our team (see Legendre & Magnaudet 1998 for details and validation). For all aspect ratios, the size of the computational domain was $55d$ in the axial direction and $32d$ in the radial direction.

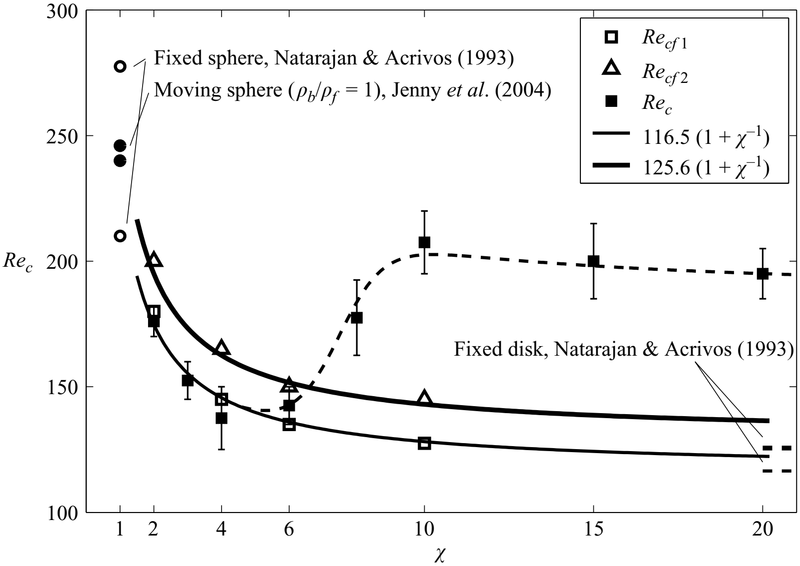

FIGURE 13. Critical Reynolds numbers characterizing the onset of instabilities: Re_{cf1}, regular bifurcation of the flow past fixed bodies (DNS); Re_{cf2}, Hopf bifurcation of the flow past fixed bodies (DNS); Re_c, onset of the path oscillations of freely rising bodies (experiment).

The three-dimensional grid was obtained by rotating a two-dimensional Cartesian grid about the body axis. The grid was made of $100 \times 66 \times 32$ elementary volumes, in the axial, radial and azimuthal directions, respectively. The grid is refined close to the body, with a first layer of cells $0.005d$ thick, which allows a satisfactory description of the boundary layer for the range of Reynolds numbers investigated (100–250). The computations are initialized with a uniform velocity, equal to the constant axial incoming velocity u_m, imposed at the top of the domain. The stability of the flow was investigated by applying a sinusoidal lateral force (y-component) in a grid cell located in the near wake. This disturbance was imposed for 1000 time steps after the initial transient stage and its amplitude was less than 1 % of the final drag force. The open symbols in figure 13 show how the two critical Reynolds numbers, Re_{cf1} and Re_{cf2}, obtained through direct numerical simulations (DNS) evolve with the aspect ratio. Both are monotonic decreasing functions of χ behaving as $1+\chi^{-1}$ and tending towards the results of Natarajan & Acrivos (1993) for a disk, $Re_{cf1} = 116.5$ and $Re_{cf2} = 125.6$, as χ tends towards infinity. The decrease in the critical Reynolds number as the body becomes thinner can be understood from an inspection of the stable attached vortex in the regime where the steady wake is stable (see figure 14). This vortex can be characterized by its maximum velocity V_w, located on the axis, and its length L_w. In order to investigate the role of the vortex intensity on the instability, we determined the value of V_w and L_w just below the onset, Re_{cf1}, of the regular bifurcation. For a given Reynolds number, both V_w/u_m and L_w/d are increasing functions of χ: the thinner the body, the more intense the attached eddy. We found that L_w/d is close to 2 and that V_w/u_m obeys $V_w/u_m \approx 0.62(1+\chi^{-1})^{-1}$. This suggests the definition of a new Reynolds number, $Re^* = V_w d/\nu$, related to the usual body Reynolds number through the empirical expression

$$Re^* = \frac{0.62}{1+\chi^{-1}} Re. \tag{5.1}$$

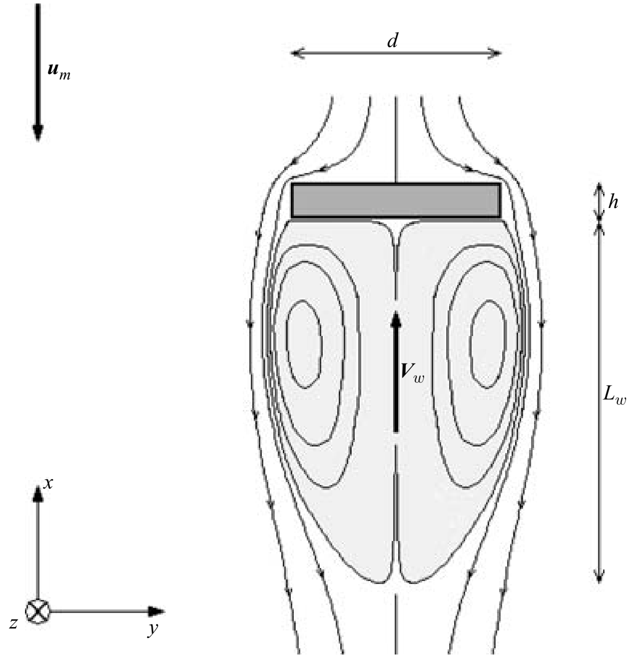

FIGURE 14. Schematic of the near wake in the body frame: V_w is the maximum recirculating velocity and L_w is the length of the closed eddy.

The great advantage of using Re^* is that the threshold of the first two bifurcations becomes independent of χ when expressed in terms of Re^*. More precisely, we now have $Re^*_{cf1} = 72$ and $Re^*_{cf2} = 78$. While quite empirical at this stage, the above choice for the definition of V_w and L_w is based on the general idea that the onset of instability is governed by the amount of vorticity generated at the body surface (Magnaudet & Mougin 2007), which is directly reflected in the characteristics of the attached eddy.

Figure 13 also shows the experimental critical Reynolds number Re_c that corresponds to the onset of the oscillatory motions of a freely rising body. Note that it might be that this threshold corresponds to a secondary bifurcation rather than to the primary one. This could be the case if the small horizontal drift that we removed from our original signals contained the signature of a primary regular bifurcation. For thick bodies ($\chi \leqslant 6$) Re_c is very close to Re_{cf1}. The corresponding body oscillations are thus controlled by the wake dynamics and start as soon as the flow axisymmetry is broken. For thin bodies ($\chi > 6$) the path instability is delayed: Re_c increases rapidly when χ rises from 6 to 10 and then seems to decrease slightly for $\chi > 10$, while Re^*_c reaches a constant value of about 116.

This behaviour of thin bodies is quite surprising since in a certain range of Re it appears that flat cylinders rise steadily whereas the wake of a fixed body of identical shape is already unsteady ($Re_c > Re_{cf2}$). This is in qualitative agreement with the early observations of Willmarth, Hawk & Harvey (1964), who noticed that falling flat disks were able to settle vertically at Reynolds numbers well beyond the threshold of the wake instability of a fixed disk. One can then wonder whether the wake of the moving body is stable in this regime. Another possibility could be that the flow is already unstable but causes only tiny oscillations of the body which are below the measurement accuracy.

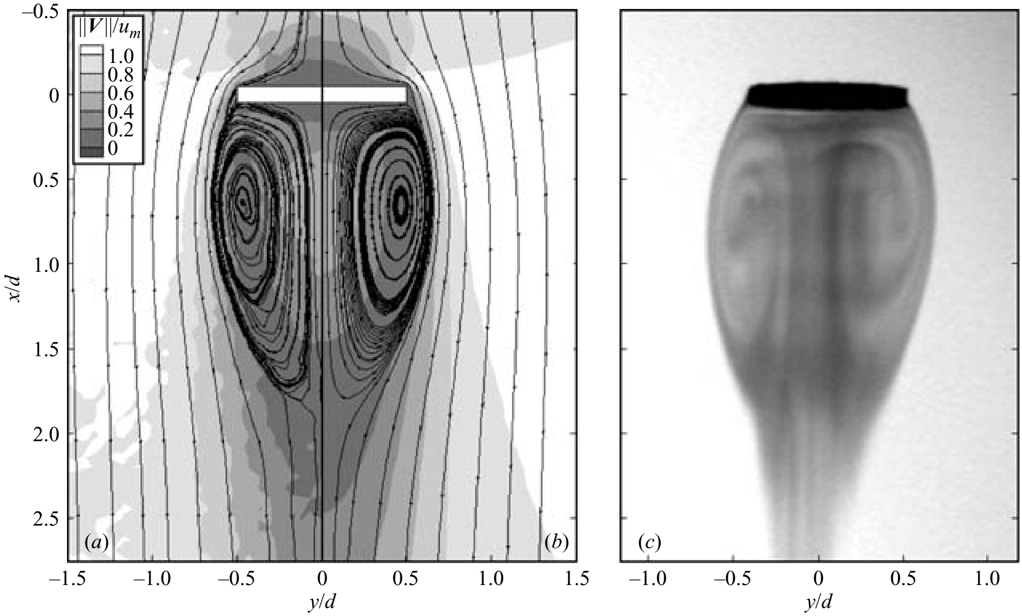

FIGURE 15. Velocity field in the laboratory frame for the steady case with $\chi = 10$ and $Re = 100 < Re_{cf1} < Re_c$. (*a*) Streamlines and velocity magnitudes around a freely rising body (from PIV); (*b*) streamlines and velocity magnitudes around a fixed body (from DNS); (*c*) dye visualization of the wake of the freely rising body.

To settle the question we used two different experimental techniques to investigate the body's wake. The first technique consists in covering the body surface with potassium permanganate, which colours the fluid while it dissolves during the body's rise. Figure 15(*c*) shows a corresponding visualization of the attached region behind the body and the streamlines within it. The second technique is the classical particle-image-velocimetry (PIV) technique. Small ($\approx 60\,\mu$m) almost neutrally buoyant ($\rho = 1.023\,\mathrm{g\,cm^{-3}}$) reflecting particles of Orgasol (2001 EXD NAT 1, ELF Atochem) were added to the fluid. A Yag laser (Twin ultra Cantel 2×30 mJ) generated a vertical sheet of light with a thickness of about 1 mm. A camera (PCO SensiCam) acquired pairs of digital images (1280×1024 pixels), the interval between the two images of each pair being 10 or 20 ms depending on the rise velocity of the body. The liquid velocity in the measurement plane was computed on a 80×64 grid from the intercorrelations of (32×32)-pixel elements by means of the PIVIS code developed in our laboratory (Cid & Gardelle 2005). Finally we obtained sequences of the velocity field in a window 60 mm wide and 48 mm high located in the region where the body motion is fully developed (see figure 15*a*). The space and time resolutions were respectively 0.05 mm and 0.25 s. Note that, since the measurement window was fixed, the sequence duration was determined by the time taken by the body to cross it, i.e. 3–6 s.

For a thin freely rising body of aspect ratio $\chi = 10$, figure 15 compares the flow field obtained by the two aforementioned experimental techniques to the fixed-body DNS prediction for $Re = 100$. Since $Re < Re_{cf1} < Re_c$, both flows are steady and must therefore be identical. Actually, the measurements are in good agreement with the DNS result; in particular the extension of the attached region is remarkably similar. After this validation, we turned to the more interesting situation where the

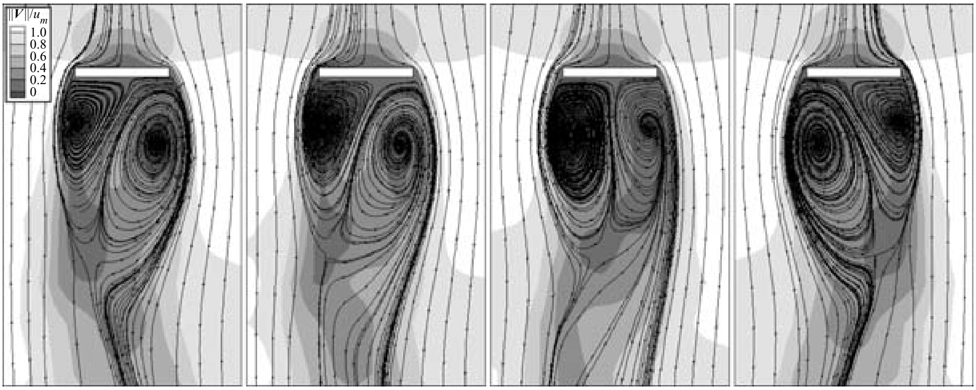

FIGURE 16. DNS of the flow about a fixed body for $\chi = 10$ and $Re_{cf1} < Re = 180 < Re_c$. The streamlines and velocity magnitudes are presented in the body frame, for the symmetry plane. The four subfigures correspond to $t = 0$, $t = T/6$, $t = T/3$ and $t = T/2$, where T is the period of the oscillations.

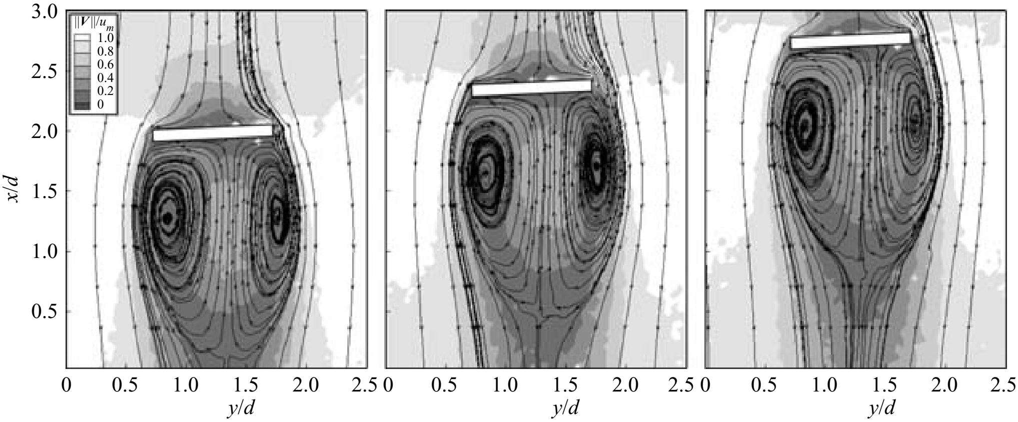

FIGURE 17. PIV measurement of the flow about a rising body for $\chi = 10$ and $Re_{cf1} < Re = 180 < Re_c$. The streamlines and velocity magnitudes are presented in the body frame, for the symmetry plane. The three subfigures correspond to $t = 0$, $t = 0.65\,d/u_m$ and $t = 1.3\,d/u_m$.

motion of the freely rising body is steady although the wake of the fixed body is unsteady: $Re_{cf2} < Re < Re_c$. Figure 16 shows the DNS around the fixed body for $Re = 180$ (the velocity field is presented in the symmetry plane xOy). Figure 17 shows the corresponding PIV measurements for the same Reynolds number (note that many tests were required to finally obtain a realization in which the symmetry plane coincided with the laser sheet). The differences between the moving and fixed bodies are obvious: the wake of the former is steady even though it is slightly asymmetric owing to a small declination of the body axis ($\approx 2°$), whereas that of the latter is clearly oscillatory (we also carried out a DNS at an inclination of 2° and did not find significant differences from the zero incidence case). The above comparison led us to conclude that, in the regime under consideration, the flow corrections induced by the extra degrees of freedom of freely moving bodies are able to suppress the wake oscillations.

For moving bodies, path and wake oscillations are always observed simultaneously and have the same frequency, as seen in figure 8. The computed frequencies of the wake oscillations of fixed bodies were also plotted in figure 8 for $\chi = 2$, 6 and 10: the corresponding Strouhal number depends weakly on both the aspect ratio and the Reynolds number. Moreover, the Strouhal number of thick moving bodies ($\chi = 2, 3$) remains very close to that of the corresponding fixed bodies whereas that of thin moving bodies ($\chi = 6, 8, 10$) is significantly larger.

Comparisons with the Strouhal and critical Reynolds numbers of the wake behind a fixed body finally led us to discern two different regimes. On the one hand, oscillations of thick bodies ($\chi < 6$) are triggered and controlled by the wake instability; the only distinctive feature of the moving bodies is that the axisymmetry and steadiness are broken simultaneously, the path oscillations starting at $Re_c = Re_{cf1}$. On the other hand, the large geometrical anisotropy of thin moving bodies ($\chi \geqslant 6$) turns out to delay the onset of wake oscillations and is responsible for the increase in their frequency when these oscillations eventually start.

6. Determination of the relevant scales

When the body is thinner, the amount of vorticity produced at its surface increases. For a body moving with a constant velocity parallel to its axis, we showed that this effect can be taken into account using the Reynolds number Re^* which characterizes the intensity of the closed vortex. For a freely rising body, changing the aspect ratio also modifies the coupling between the body's translational and rotational degrees of freedom; in particular, the anisotropy of the proper and added-inertia tensors strongly depends on χ. In this section we consider all the parameters characterizing the body motion in the rotating frame as functions of Re^* (defined by (5.1)) in order to make clear the role of the degrees of freedom. Our strategy consists in looking for the time, velocity and length scales that allow the results corresponding to the various aspect ratios to collapse onto a master curve.

We know from figure 8 that $u_m d^{-1}$ (or $u_g d^{-1}$) is not the relevant scale for normalizing the frequency f of the oscillations. Therefore let us define another Strouhal number, namely

$$St^* = \frac{fd}{\sqrt{(\Delta\rho/\rho)gd}} = St(2/C_d)^{1/2}\chi^{-1/2}. \tag{6.1}$$

Figure 18 shows that St^* is almost independent of both the Reynolds number and the aspect ratio: $St^* \approx 0.10$. Mahadevan *et al.* (1999), from experiments with falling cards, and Jones & Shelley (2005), from numerical computations of the Euler equations around a moving card, found that St is proportional to $\chi^{1/2}$, which is equivalent to the present result. We have seen already that the oscillation frequency of thick moving bodies is close to the shedding frequency of fixed bodies of identical shape (see figure 8), which is almost independent of χ. Moreover, St^* approximately equals St for $\chi = 1.5$. For all aspect ratios and Reynolds numbers, the value of St^* for a given moving body is therefore close to that of St for its fixed counterpart.

Figure 19 shows the evolution of the amplitude of the body-axis inclination. This figure is similar to figure 10 but here $\widetilde{\theta}_y$ is plotted against Re^* instead of Re. For thick bodies ($\chi \leqslant 6$), the amplitudes nicely collapse onto a single curve,

$$\widetilde{\theta}_y = 5.8 \times 10^{-2}(Re^* - Re^*_{cf1})^{1/2} = f_{\theta_y}(Re^*), \tag{6.2}$$

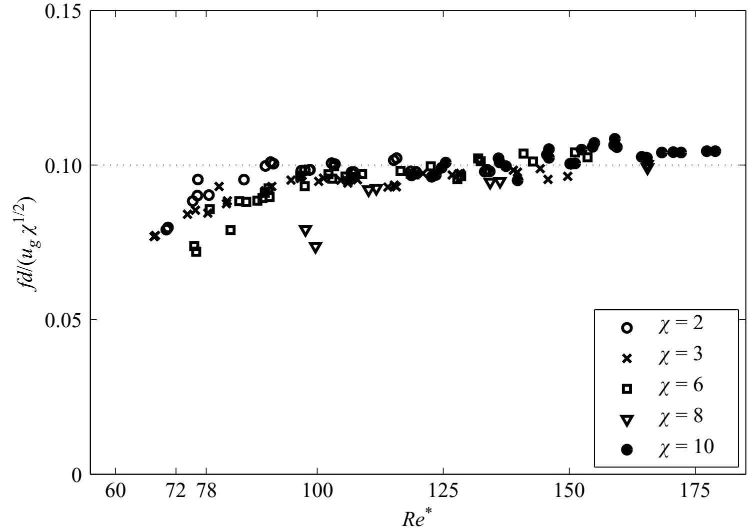

FIGURE 18. Modified Strouhal number $St^* = fd/\sqrt{(\Delta\rho/\rho_f)gd}$ vs. Re^* for $\chi = 2$, 3, 6, 8 and 10.

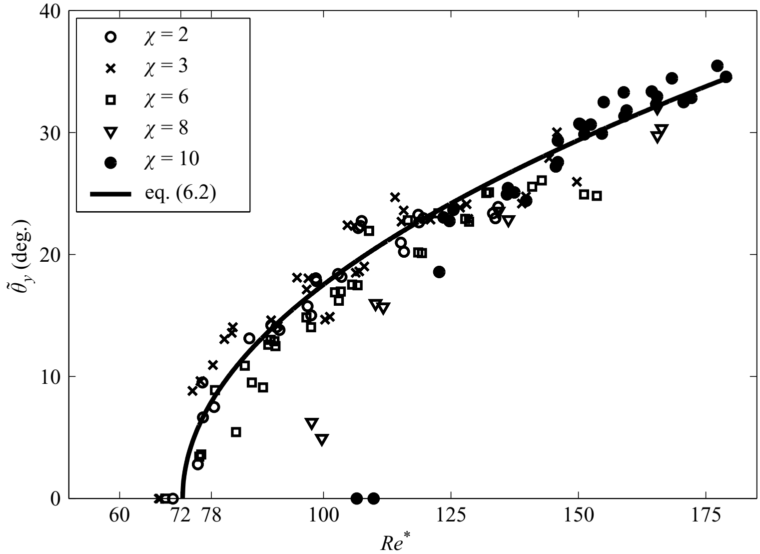

FIGURE 19. Amplitude of the body-axis inclination $\widetilde{\theta}_y$ vs. Re^* for $\chi = 2$, 3, 6, 8 and 10.

which is probably the signature of a supercritical Hopf bifurcation. We already know that the threshold of the path instability of thick bodies does not depend on the aspect ratio ($Re_c^* = Re_{cf1}^*$); for $Re^* > Re_c^*$ we now see that the increase in their amplitude is also independent of χ. For thin bodies ($\chi \geqslant 6$), the onset is delayed ($Re_c^* > Re_{cf1}^*$), so that the amplitudes cannot collapse with those of thick bodies over the whole range of Re^*. However, beyond the onset, the values of $\widetilde{\theta}_y$ for $\chi = 8$ and 10 rapidly join the other results on the curve defined by (6.2). For $\chi = 10$, we did not manage to measure small amplitudes just beyond the onset and $\widetilde{\theta}_y$ seems to jump directly from zero to a finite value located on curve (6.2), which could correspond to a subcritical

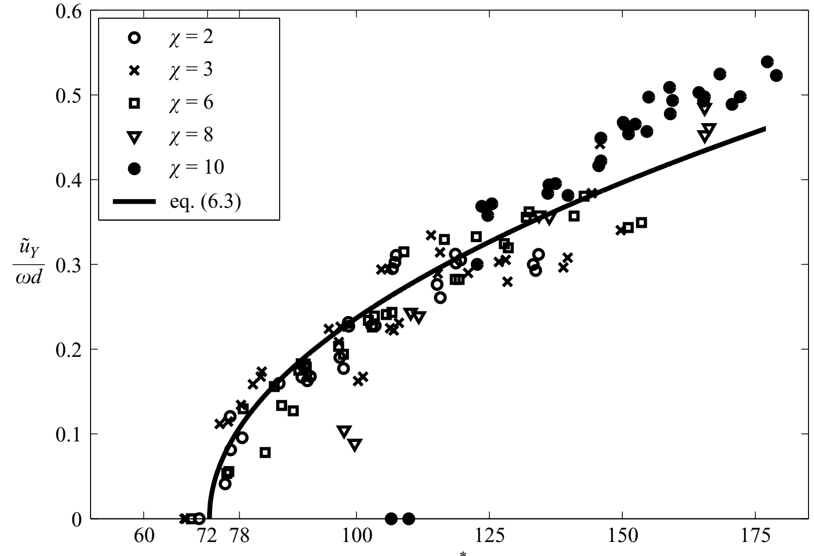

FIGURE 20. Normalized amplitude of the lateral velocity, $\widetilde{u_Y}/\omega d$, vs. Re^* for $\chi = 2$, 3, 6, 8 and 10.

bifurcation. This makes us wonder whether, for thin bodies, the bifurcation remains supercritical or becomes subcritical. Accurate measurements close to the onset are unfortunately difficult; the smaller the amplitude, the more difficult it is to disentangle regular oscillations from perturbations due to the small residual large-scale motions, and the longer the time needed to relax towards saturation. Therefore the present experiments do not allow us to settle the above question. Direct numerical simulation is probably a more appropriate tool to elucidate the nature of the bifurcation, as used by Mougin & Magnaudet (2002) for a rising bubble. In the laboratory frame, the amplitude of the horizontal displacement, $\tilde{y}$, normalized by the body diameter d strongly depends on the aspect ratio. Figure 20 shows the amplitude of the lateral velocity, $\widetilde{u_Y}$, in the rotating frame, normalized by ωd. Note that since we consider harmonic functions, scaling the velocity by ωd is strictly equivalent to scaling the displacement by d. As for $\tilde{\theta}_y$, the values of $\widetilde{u_Y}/\omega d$ collapse onto a single curve,

$$\frac{\widetilde{u_Y}}{\omega d} = 4.5 \times 10^{-2}(Re^* - Re^*_{cf1})^{1/2} = f_{u_Y}(Re^*). \tag{6.3}$$

This confirms that the rotating frame is better suited than the laboratory frame for studying the body dynamics. From the scaling of the frequency ($St^* \approx 0.1$) and (6.3), we obtain $\widetilde{u_Y} \approx 0.2\pi\sqrt{(\Delta\rho/\rho_f)gd}\, f_{u_Y}(Re^*)$. It is also worth noting that, when correctly normalized, the two oscillating quantities θ_y and u_Y have the same onset, frequency and amplitude over the whole range of parameters investigated. They are thus two signatures of the same instability and it is equivalent to study the nature of the bifurcation from either of them. However, their relative dynamics remain complex. Figure 21 presents the evolutions of their phase difference ϕ_Y as a function of Re^*. Qualitatively, the behaviour of ϕ_Y is similar to that of $\Delta\phi$, the phase difference between the velocity and orientation in the laboratory frame: ϕ_Y significantly increases with χ whereas it only weakly increases with Re^*. However, the range of variation in

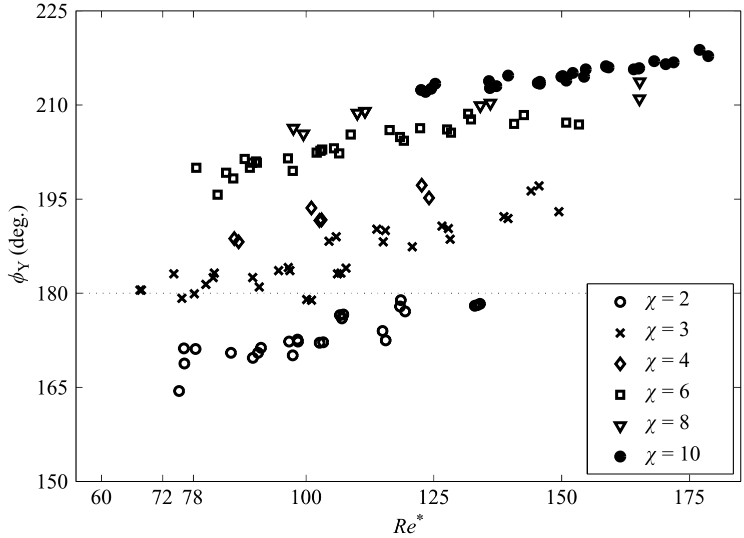

FIGURE 21. Phase difference ϕ_Y vs. Re^* for $\chi = 2$, 3, 4, 6, 8 and 10.

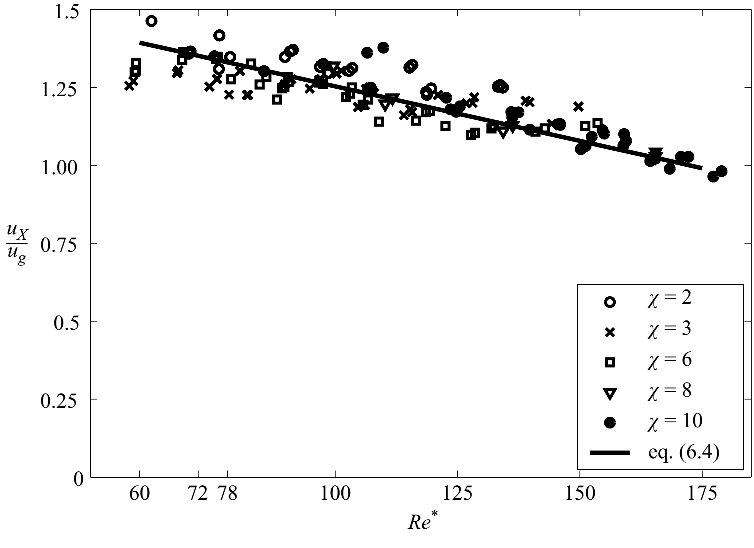

FIGURE 22. Constant axial velocity, $u_X = \overline{u_X}$, vs. Re^* for $\chi = 2$, 3, 6, 8 and 10.

ϕ_Y is only half that in $\Delta\phi$ (60° instead of 120°), with values spreading around 180°. We did not find any relevant scaling for expressing the variation in ϕ_Y with χ.

Figure 22 shows the constant axial velocity $\overline{u_X}$, normalized by the gravitational velocity u_g. The results found for all aspect ratios collapse onto a single curve,

$$\frac{\overline{u_X}}{u_g} = 1.35 - 3.5 \times 10^{-3}(Re^* - Re^*_{cf1}), \tag{6.4}$$

which exhibits a slight decrease with Re^*, from approximately $\overline{u_X} = 1.4$ for $Re^* = 60$ down to 1 for $Re^* = 175$.

The relevant scales are thus made clear in the body frame. On the one hand, the constant axial velocity scales as $u_g = \sqrt{(\Delta\rho/\rho_f)\, gh}$, like the mean rise velocity. On the other hand, the length, velocity and time scales of the body oscillations are d, $\sqrt{(\Delta\rho/\rho_f)\, gd} = u_g\chi^{1/2}$ and the ratio of these two quantities, respectively. The body motion is thus defined by five dimensionless parameters: $\widetilde{\theta}_y$, $\widetilde{u_Y} u_g^{-1}\chi^{-1/2}$, $\overline{u_X} u_g^{-1}$, St^*, which are functions of Re^* only, and ϕ_Y, which depends on both χ and Re^*.

7. Conclusion

We performed an experimental study of the kinematics of freely rising oblate axisymmetric bodies. The density ratio was maintained close to unity to focus on the roles of the Reynolds number and the aspect ratio. We explored the range of parameters where either a rectilinear rise at a constant velocity or a regular oscillatory motion are expected. We first showed that the body motion is essentially two-dimensional and thus we can reduce its description to the evolution of three degrees of freedom, two in translation and one in rotation. We then observed that the behaviour looks much simpler in a coordinate system rotating with the body in which the axial velocity is constant. Since we observed that the body's rotation and lateral velocity are harmonic functions of time, the description of the body motion could be reduced to only five parameters (see (4.1)–(4.3)). From comparisons with the threshold and the shedding frequency of fixed-body wakes, we distinguished the behaviours of thick ($\chi < 6$) and thin bodies ($\chi \geqslant 6$). On the one hand, the degrees of freedom of thick moving bodies play a minor role in the dynamics. The effect of the aspect ratio is restricted to its role in the vorticity production at the body surface and can be taken into account by introducing a new Reynolds number, Re^* (5.1), which may be thought of as being based on the maximum vorticity in the near wake. On the other hand, the flow corrections induced by the translational and rotational degrees of freedom of thin moving bodies are able to delay the onset of oscillations. We investigated the evolution of the motion parameters in the rotating frame as a function of Re^* and found that the relevant length and velocity scales of the oscillations are respectively d and $\sqrt{(\Delta\rho/\rho_f)\, gd}$. When made dimensionless using these scales, the frequency and amplitude of the oscillations are almost independent of χ.

The body kinematics have been investigated in detail in this work. We now have to understand the underlying dynamics that govern the observed scalings. This implies an investigation of the hydrodynamic forces acting on the body and their coupling to the body's degrees of freedom, which will be the subject of a forthcoming paper.

This work was supported by an ACI Jeunes Chercheurs of the French Ministry of Research. We are grateful to D. Fabre for his help with the numerical simulations. We also thank H. Ayroles, S. Cazin, E. Cid, N. Rollin, C. Trupin, J.-J. Huc and J.-P. Escafit for technical assistance.

REFERENCES

Andersen, A., Pesavento, U. & Wang, Z. J. 2005*a* Unsteady aerodynamics of fluttering and tumbling plates. *J. Fluid Mech.* **541**, 65–90.

Andersen, A., Pesavento, U. & Wang, Z. J. 2005*b* Analysis of transitions between fluttering, tumbling and steady descent of falling cards. *J. Fluid Mech.* **541**, 91–104.

Aybers, N. M. & Tapucu, A. 1969 The motion of gas bubbles rising through a stagnant liquid. *Wärme- und Stoffübertragung* **2**, 118–128.

Belmonte, A., Eisenberg, H. & Moses, E. 1998 From flutter to tumble: inertial drag and Froude similarity in falling paper. *Phys. Rev. Lett.* **81**, 345–348.

Cid, E. & Gardelle, F. 2005 Manuel d'utilisation du logiciel PIVIS. *Tech. Rep.* Institut de Mécanique des Fluides de Toulouse.

Ellingsen, K. & Risso, F. 2001 On the rise of an ellipsoidal bubble in water: oscillatory paths and liquid-induced velocity. *J. Fluid Mech.* **440**, 235–268.

Fernandes, P. C., Ern, P., Risso, F. & Magnaudet, J. 2005 On the zigzag dynamics of freely moving axisymmetric bodies. *Phys. Fluids* **17**, 098107.

Field, S., Klaus, M., Moore, M. & Nori, F. 1997 Chaotic dynamics of falling disks. *Nature* **388**, 252–254.

Ghidersa, B. & Dusek, J. 2000 Breaking of axisymmetry and onset of unsteadiness in the wake of a sphere. *J. Fluid Mech.* **423**, 233–269.

Jenny, M., Dusek, J. & Bouchet, G. 2003 Nonvertical ascension or fall of a free sphere in a Newtonian fluid. *Phys. Fluids* **15**, L9–L12.

Jenny, M., Dusek, J. & Bouchet, G. 2004 Instabilities and transition of a sphere falling or ascending in a Newtonian fluid. *J. Fluid Mech.* **508**, 201–239.

Johnson, T. A. & Patel, V. C. 1999 Flow past a sphere up to a Reynolds number of 300. *J. Fluid Mech.* **378**, 19–70.

Jones, M. A. & Shelley, M. J. 2005 Falling cards. *J. Fluid Mech.* **540**, 393–425.

Lamb, H. 1932 *Hydrodynamics*, 6th edn. Cambridge University Press.

Legendre, D. & Magnaudet, J. 1998 The lift force on a spherical bubble in a viscous linear shear flow. *J. Fluid Mech.* **368**, 81–126.

Magnaudet, J. & Mougin, G. 2007 Wake instability of a fixed spheroidal bubble. *J. Fluid Mech.* **572**, 311–338.

Mahadevan, L. 1996 Tumbling of a falling card. *C. R. Acad. Sci. Paris* II **323**, 729–736.

Mahadevan, L. , Ryu, W. & Samuel, A. 1999 Tumbling cards. *Phys. Fluids* **11**, 1–3.

Mougin, G. & Magnaudet, J. 2002 Path instability of a rising bubble. *Phys. Rev. Lett.* **88**, 14502.

Natarajan, R. & Acrivos, A. 1993 The instability of the steady flow past spheres and disks. *J. Fluid Mech.* **254**, 323–344.

Pesavento, U. & Wang, Z. J. 2004 Falling paper: Navier-Stokes solutions, model of fluid forces, and center of mass elevation. *Phys. Rev. Lett.* **93**, 144501.

Provansal, M. & Ormières, D. 1998 Étude expérimentale de l'instabilité du sillage d'une sphère. *C. R. Acad. Sci., Ser.* IIb **326**, 11–22.

Saffman, P. G. 1956 On the rise of small air bubbles in water. *J. Fluid Mech.* **1**, 249–275.

Schouveiler, L. & Provansal, M. 2002 Self-sustained oscillations in the wake of a sphere. *Phys. Fluids* **14**, 3846–3854.

Stewart, R. E. & List, R. 1983 Girational motion of disks during free fall. *Phys. Fluids* **26**, 920–927.

Willmarth, W., Hawk, N. & Harvey, R. 1964 Steady and unsteady motions and wakes of freely falling disks. *Phys. Fluids* **7**, 197–208.

Wolf, A. V., Brown, M. G. & Prentiss, P. G. 1981 Concentrative properties of aqueous solutions: conversion tables. *CRC Handbook of Chemistery and Physics*, D-227, 61st edn. CRC Press.